J Braz Comput Soc (2011) 17:117–132
DOI 10.1007/s13173-011-0032-8

ORIGINAL PAPER

Detection of point landmarks in 3D medical images via phase congruency model

Ricardo J. Ferrari · Stéphane Allaire · Andrew Hope · John Kim · David Jaffray · Vladimir Pekar

Received: 16 September 2010 / Accepted: 28 February 2011 / Published online: 19 March 2011

Abstract This paper presents a novel technique for detection of point landmarks in volumetric medical images based on a three-dimensional (3D) Phase Congruency (PC) model. A bank of 3D log-Gabor filters is specially designed in the frequency domain and used to compute 3D energy maps, which are further combined to form the phase congruency measure. The PC measure is invariant to intensity variations and contrast resolution and provides a good indication of feature significance in an image. To detect significant 3D point landmarks, eigen-analysis of a 3×3 matrix of second-order PC moments, computed for each point in the image, is performed followed by local maxima detection. Two different application scenarios in radiation therapy planning of the head and neck anatomy are used to illustrate the feasibility and usefulness of the proposed method.

Keywords Point landmarks · 3D hase congruency · 3D log-Gabor filters · Wavelets · Nonrigid registration · Radiation therapy

R.J. Ferrari (✉)
Department of Computer Sciences, Federal University of São Carlos (UFSCar), Rod. Washington Luís, Km 235, Caixa Postal 676, 13565-905 São Carlos, SP, Brazil
e-mail: rferrari@dc.ufscar.br

S. Allaire · A. Hope · J. Kim · D. Jaffray
Princess Margaret Hospital, University of Toronto, Toronto, ON, Canada

V. Pekar
Philips Research North America, Toronto, Markham, ON, Canada

1 Introduction

Detection of distinctive 3D anatomical point landmarks is an important task in a variety of medical image analysis applications including image-to-image and atlas-to-image registration. Landmark-based registration usually comprises three main steps: (1) detection of reliable landmarks in datasets to be registered; (2) establishment of correspondences between the landmarks; and (3) determination of the transformation between the datasets using the landmark correspondences. Usually, the localization of anatomical point landmarks in medical images is carried out manually by an expert physician. However, manual annotation of image landmarks, especially in 3D images, is a time-consuming and error-prone task, and in general it presents high inter-observer variability and low reproducibility [17]. Therefore, there is a great interest in developing automatic techniques that could reliably detect 3D landmarks in medical image.

In this work, a new technique for detection of 3D point landmarks in medical images based on an implementation of the 3D PC model is proposed. The intrinsic image contrast invariance as well as the good spatial and frequency localization provided by the log-Gabor filters make the proposed method very suitable for applications in medical image analysis. In addition to the landmarks, the method also provides 3D PC maps, which correspond to important visual salient features in an image and can be used, for instance, to replace image intensity information in image registration applications, e.g., multimodality registration [46].

The paper is organized as follows: Section 2 describes the related previous work presented in the literature; the methodology of the proposed method is described in Sect. 3, followed by two different application scenarios in Sect. 4 that are used to illustrate the feasibility and usefulness of the 3D PC-landmarks algorithm. Conclusions are presented in Sect. 5.

2 Previous work

A handful of papers have been presented in the literature addressing the problem of detection of 3D medical image landmarks. Monga and Benayoun [30] proposed a method based on 3D partial derivatives of the image to estimate local curvature of isosurfaces. The gradient direction is then used to find the tangent plane of the isosurface at each point in an image. Principal curvatures and their directions are computed by maximizing a criterion derived from the Hessian matrix over the tangent plane direction. Thirion [41] applied partial derivatives to detect crest lines, or loci of the surface, where the curvature is locally maximal. Geometrical invariants are then used to determine the external points, which are further applied to image coregistration. Rohr [37] has extended to 3D four of the two-dimensional (2D) curvature operators based on second-order partial derivatives, which were previously proposed in the literature [11, 18]. Other metrics computed from the Hessian matrix were also investigated by the author. Ruiz-Alzola et al. [38] proposed a method based on the interpretation of generalized correlation matrices derived from the gradient of tensor functions, a probabilistic interpretation of point landmarks, and the application of tensor algebra. The landmarks are detected as local maxima of a function defined by the determinant of a generalized correlation matrix over its trace. Wörz and Rohr [47] have also proposed 3D parametric intensity models for the localization of 3D anatomical point landmarks in brain images. Their method uses differential properties of the image (e.g., gradient and curvature) and a fitting scheme based on the least-squares method in order to fit their parametric models to the landmarks. Three types of structures were considered by the proposed models: tip-, saddle-, and sphere-like structures. Cheung and Hamarneh [4] have extended to n-dimension the Scale Invariant Feature Transform (SIFT) commonly used in computer vision. The authors have proposed three SIFT-like features computed from local intensity histogram re-oriented in the direction of local gradients for matching points between brains MRI of different modalities. Allaire et al. [1] have also proposed a technique to detect 3D anatomical landmarks based on a 3D extension of the SIFT. The authors have introduced a new efficient procedure for selection of salient features based on the analysis of the 3×3 Hessian matrix. By normalizing the histograms of local gradient orientations with respect to the dominant 3 angles (azimuth, elevation, and tilt), the landmark feature descriptor achieves full orientation invariance. More recently, Liu et al. [24] have proposed a new model-based, semiglobal segmentation approach to automatically localize 3D point landmarks in neuroimages. In their work, a landmark is localized by first using an active surface model applied only to a part of the studied structure in a certain neighborhood of the landmark, and then analyzing the segmented part. By combining global model-to-image registration, semi-global structure registration, active surface-based segmentation, and point-anchored surface registration, the authors claim that their method is robust to noise and shape variation.

Although a direct quantitative comparison of the method proposed in this paper and all other available approaches for the detection of 3D landmarks presented in the literature is an almost infeasible task, due to the lack of details provided to implement and test all the algorithms, a brief comparison of the proposed method and the well-known SIFT technique is presented as follows.

The main advantages of our proposed method for detection of anatomical point landmarks in comparison to the SIFT technique are: (a) differently to the SIFT technique, the PC measure is very robust to intensity variations in an image, since it is based on the local energy model of feature perception [31] and not in points located at the local extrema of derivative images; (b) the proposed method does not require any post-processing stage to eliminate unlikely local extrema and to make the features invariant to rotation; (c) although the current implementation of the proposed method has a higher computational cost comparing to the SIFT technique, its performance can be greatly improved via a Graphic Processing Unit (GPU) [39] implementation of the filtering process or even using a downscaling implementation of the algorithm in frequency domain with time complexity of $O(N \log N)$; (d) last but not least, the proposed method does not have any patent license restrictions as SIFT does.

3 Methodology

The phase congruency model provides a measure of feature significance that is invariant to intensity variations and contrast resolution in an image [21]. It was first proposed by Morrone et al. [33] in terms of the Fourier series for the 1D signal case to explain the paradoxical Match band phenomenon. Rather than assuming that a feature is a point of maximal intensity gradient, the phase congruency model postulates that features are perceived at points in an image where the Fourier components are maximally in phase. Besides the fact that this model successfully explains a number of psycho-physical effects in human feature perception, it also provides a robust measure against image intensity variations, once it is based mainly on the phase information of a signal. Venkatesh and Ownes [43] have shown that the phase congruency measure is proportional to the local energy model. They also suggested calculating the local energy via convolution of the original signal with a set of spatial filters in quadrature.

Fairly recently, three different measures of phase congruency (PC1, PC2, and PC3) for application in 2D images have been proposed [20, 45]. These measures have shown to provide very good feature localization and have been used in different 2D medical image processing tasks [3, 8, 23, 29, 40, 45]. In this work, a 3D extension of the PC2 measure was developed using a bank of quadrature pairs of 3D log-Gabor filters proposed by Dosil et al. [7]. To the authors' best knowledge, this is the first time this technique is used to detect 3D landmarks in medical images. The new 3D PC-measure is defined as

$$\mathrm{PC}_{3\mathrm{D}}(\mathbf{s},\Theta)=\frac{\sum_n W(\mathbf{s},\Theta)\,\lfloor A_n(\mathbf{s},\Theta)\Delta\Phi_n(\mathbf{s},\Theta)-T\rfloor}{\sum_n A_n(\mathbf{s},\Theta)+\epsilon}, \tag{1}$$

where $\lfloor\cdot\rfloor$ denotes that the enclosed quantity is equal to itself when its value is positive, and zero otherwise; $\mathbf{s}$ indicates a spatial location (x, y, z) in an image, and $\Theta=(\theta,\phi)$ gives the filter orientation on a sphere of unit radius, with θ and ϕ corresponding respectively to the elevation and azimuth angles. $A_n(\mathbf{s},\Theta)$ indicates the image energy at location $\mathbf{s}$, computed by using a 3D log-Gabor filter with scale index n and orientation Θ. The index n varies from 1 to S, the total number of scales being used, which was set to 3 in this work. T is a threshold controlling the noise level of the image energy map and ϵ is a small constant to avoid division by zero. Clearly, a point of phase congruency is only significant if it occurs over a wide range of frequencies [19, 20, 31, 32]. In a degenerate case where there is only one frequency component in a signal, the phase congruency measure, which varies from 0 to 1, will be one everywhere. The term $W(\mathbf{s},\Theta)$, defined as

$$W(\mathbf{s},\Theta)=\frac{1}{1+e^{\gamma(c-l(\mathbf{s},\Theta))}}, \tag{2}$$

was devised by Kovesi [19] as a weighting function that penalizes frequency distributions that are particularly narrows. The parameters γ and c in this function are constants representing a gain factor and a cut-off value, respectively, and

$$l(\mathbf{s},\Theta)=\frac{1}{S}\left(\frac{\sum_n A_n(\mathbf{s},\Theta)}{A_{\max}(\mathbf{s},\Theta)+\epsilon}\right) \tag{3}$$

is a measure of filter response spread computed as the sum of the amplitudes of the responses (A_n) divided by the highest individual response ($A_{\max}$) in order to obtain some notional "width" of the distribution.

The original phase congruency proposed by Morrone and Burr [31] suffered from a poor localization on blurred features. The reason is that energy is proportional to the cosine of the deviation of the phase angle, $\phi_n(\mathbf{s},\Theta)$, from the overall mean phase angle, $\overline{\phi}_n(\mathbf{s},\Theta)$. While the cosine function is maximized when $\phi_{\mathbf{s},\Theta}=\overline{\phi}_n(\mathbf{s},\Theta)$, it requires a significant difference between these terms before its value falls considerably. To minimize the lack of localization in the original phase congruency measure, a new energy expression was proposed by Kovesi [19] as

$$\begin{aligned}\Delta\Phi_n(\mathbf{s},\Theta)&=\cos\big(\phi_n(\mathbf{s},\Theta)-\overline{\phi}_n(\mathbf{s},\Theta)\big)\\&\quad-\big|\sin(\phi_n(\mathbf{s},\Theta)-\overline{\phi}_n(\mathbf{s},\Theta))\big|\\&=e_n(\mathbf{s},\Theta)\overline{\phi}_e(\mathbf{s},\Theta)+o_n(\mathbf{s},\Theta)\overline{\phi}_o(\mathbf{s},\Theta)\\&\quad-\big|e_n(\mathbf{s},\Theta)\overline{\phi}_o(\mathbf{s},\Theta)-o_n(\mathbf{s},\Theta)\overline{\phi}_e(\mathbf{s},\Theta)\big|,\end{aligned} \tag{4}$$

where

$$\overline{\phi}_e(\mathbf{s},\Theta)=\sum_n e_n(\mathbf{s},\Theta)/E(\mathbf{s},\Theta),$$

$$\overline{\phi}_o(\mathbf{s},\Theta)=\sum_n o_n(\mathbf{s},\Theta)/E(\mathbf{s},\Theta),\quad\text{and}$$

$$E(\mathbf{s},\Theta)=\sqrt{\left(\sum_n e_n(\mathbf{s},\Theta)\right)^2+\left(\sum_n o_n(\mathbf{s},\Theta)\right)^2}.$$

The term $E(\mathbf{s},\Theta)$ is the local energy and $e_n=I\bullet G_n^e$ and $o_n=I\bullet G_n^o$ are the convolution results of the input image I with the quadrature even and odd 3D log-Gabor pairs of filters G_n^e and G_n^o, respectively, at scale n and orientation Θ. This formulation takes into account the fact that, at a point of phase congruency, the cosine of the phase deviation should be large and the absolute value of the sine of the phase deviation should be small.

3.1 Design of the 3D log-Gabor filters

The bank of complex 3D log-Gabor filters was designed in the Fourier domain based on the work of Dosil et al. [7], and it was used for the implementation of the phase congruency technique as described previously. The choice for log-Gabor filters is two fold: (i) log-Gabor filters have zero DC component[1] and, therefore, do not respond to regions with constant gray value intensities; (ii) the filters have extended tails covering high frequencies, thus making possible to obtain arbitrarily wide bandwidth, which can yield to a fairly uniform coverage of the frequency domain in an octave scale multiresolution scheme. For the reasons mentioned above, it has also been suggested that the log-Gabor function should be able to encode natural images more efficiently than the ordinary Gabor functions, frequently used in the literature for image filtering [9, 10].

In 1D, a log-Gabor function has a transfer function of the following form

$$R_i(\omega)=\exp\left\{-0.5\cdot\frac{\ln^2\left(\frac{\omega}{\omega_i}\right)}{\ln^2\left(\frac{\sigma_\beta}{\omega_i}\right)}\right\}, \tag{5}$$

[1] Value corresponding to offset component of the spectrum of an image.

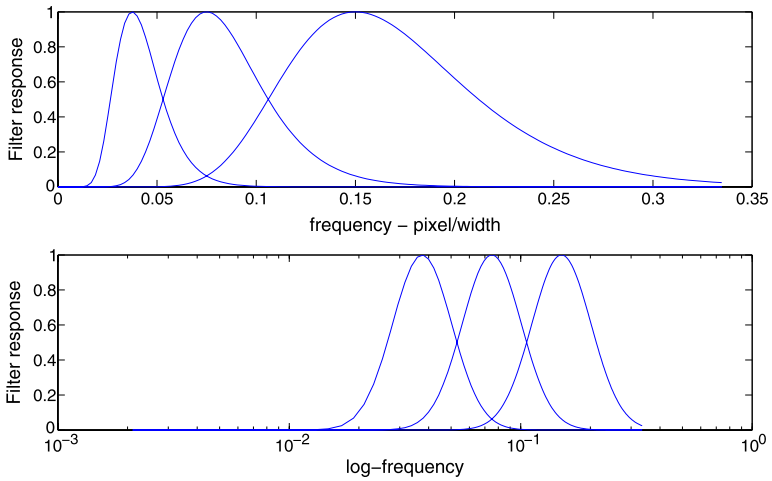

Fig. 1 Design of the radial component of the bank of log-Gabor filters for the linear and logarithm frequency scales for 3 scales (wavelengths of approximately 7, 14, and 28 pixels), one octave bandwidth ($\eta_\beta = 0.745$) and maximum radial centre frequency set to $\omega_{\max} = 0.15$. The *bottom subplot* shows the filters uniformly covering the spectrum

where ω_i is the central radial frequency of the filter i and σ_β is the standard deviation controlling the filter bandwidth [10]. To obtain constant shape ratio filters, i.e., filters that are all geometric scaling of a reference filter (referred to mother wavelet in the wavelets' literature), the term $\frac{\sigma_\beta}{\omega_i}$ must be held constant for varying ω_i. It can be shown that $\frac{\sigma_\beta}{\omega_i}$ is related to the filter bandwidth β by the following expression $\eta_\beta = \frac{\sigma_\beta}{\omega_i} = \exp(-\frac{1}{4}\sqrt{2\ln 2}\beta)$, with $0 < \eta_\beta < 1$ and β given in octaves [6]. Figure 1 shows the radial components of the log-Gabor filters used in this work.

To extend the filters to 3D, a Gaussian on the angular distance, which has rotational symmetry in spherical coordinates, is used to control the spread of the angular frequency component as given by

$$G(\Theta) = \exp\left(-0.5 \cdot \frac{\alpha(\Theta)^2}{\sigma_\alpha^2}\right), \tag{6}$$

where σ_α is the angular standard deviation of the filter and $\alpha(\Theta) = \arccos(\frac{\omega \cdot \mathbf{u}}{\|\mathbf{u}\|})$, with $\mathbf{u} = (\cos\theta \cdot \cos\phi, \cos\theta \cdot \sin\phi, \sin\theta)$ and ω is a point in the frequency space expressed in Cartesian coordinates.

By multiplying the radial and angular components given respectively by (5) and (6), the 3D log-Gabor transfer function is obtained as

$$T(\omega, \Theta) = \exp\left\{-0.5 \cdot \frac{\ln^2\left(\frac{\omega}{\omega_i}\right)}{\ln^2(\eta_\beta)}\right\} \cdot \exp\left(-0.5 \cdot \frac{\alpha(\Theta)^2}{\sigma_\alpha^2}\right). \tag{7}$$

In the current implementation of the bank of log-Gabor filters, elevation is uniformly sampled while the number of azimuth angles (N_a) decreases with elevation in order to keep the density of filters constant. This is achieved by keeping an equal arc-length between adjacent azimuth values over the unit radius sphere instead of taking uniform angular distances [7]. Therefore, the number of filters vary with the elevations as

$$N_a = \sum_{i=1}^{N_e} N_{a,0} \cdot \cos\left(i \cdot \frac{\pi}{2N_e}\right), \tag{8}$$

where $N_{a,0}$ is the number of azimuth angles in the equator of the unit radius sphere (please refer to Fig. 2) and N_e is the number of elevations.

The filter design also allows to sample the angular frequency space in a uniform or nonuniform mode, as illustrated in Fig. 2. This 3D log-Gabor filter representation has the advantage of being flexible in controlling the number of filters in the equator of the sphere, which are the orientations that fall in the xy-plane. This is especially important in the case of medical images in which the slice thickness is usually larger than the in-slice resolution. In addition, by allowing nonuniform sampling, the number of filters can be considerably reduced in this representation, which reduces the computational time for processing an image.

3.1.1 Implementation details

In order to reduce the computational burden involved in the convolution of the original image with the even G_n^e and odd G_n^o parts of each log-Gabor filter, which would require two inverse Fourier transformations, in this proposed filter design G_n^e and G_n^o are combined as one complex filter as $\hat{G}_n = G_n^e + iG_n^o$. Subsequently, by exploiting the linearity of the Fourier transform, where $\mathrm{FFT}(A+B) = \mathrm{FFT}(A) + \mathrm{FFT}(B)$, if this filter is multiplied by the Fast Fourier Transform (FFT) of the image I and an inverse Fourier transform is applied to the result, then the real and imaginary parts of the result will correspond, respectively, to $e_n = I \bullet G_n^e$ and $o_n = I \bullet G_n^o$, where $\bullet$ indicates the convolution operator. This halves the number of inverse Fourier transforms required to process an image. It should also be noted that in the frequency domain the even- and odd-symmetric filters

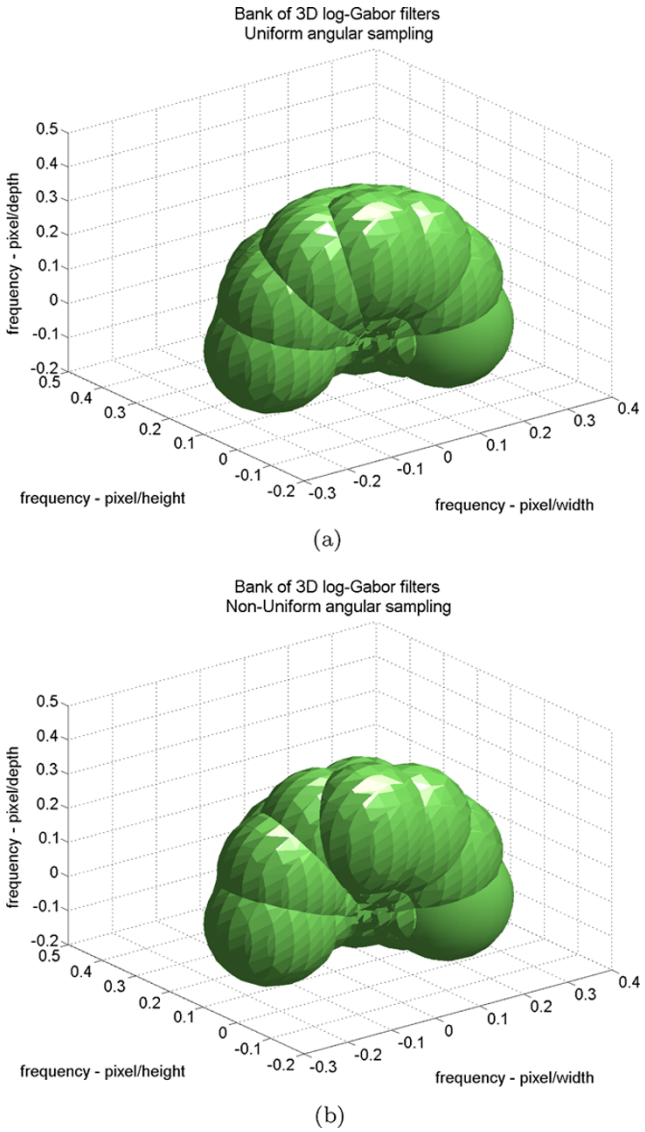

Fig. 2 Bank of 3D log-Gabor filters designed (**a**) *with* and (**b**) *without* uniform sampling on the angular frequency space. An angular oversampling around the pole (elevation angle of $\frac{\pi}{2}$) can be noticed in (**a**). The number of filters used to cover the Fourier spectrum in (**a**) and (**b**) are 75 and 45, respectively

are represented, respectively, by two symmetric real and two antisymmetric imaginary valued log-Gaussian "blobs" symmetrically placed on each side of the origin. Due to the opposing symmetries, an antisymmetric "blob" from the odd-symmetric filter will cancel out the corresponding symmetric "blob" from the even-symmetric filter resulting in a single real-valued "blob" (multiplied by 2) on the positive side of the frequency spectrum [36].

Figure 3 illustrates a log-Gabor filter designed in the frequency domain and the corresponding isosurfaces of the even and odd filters in the spatial domain.

In this work, the bank of 3D log-Gabor filters is computed off-line. For each filter, the envelop corresponding to

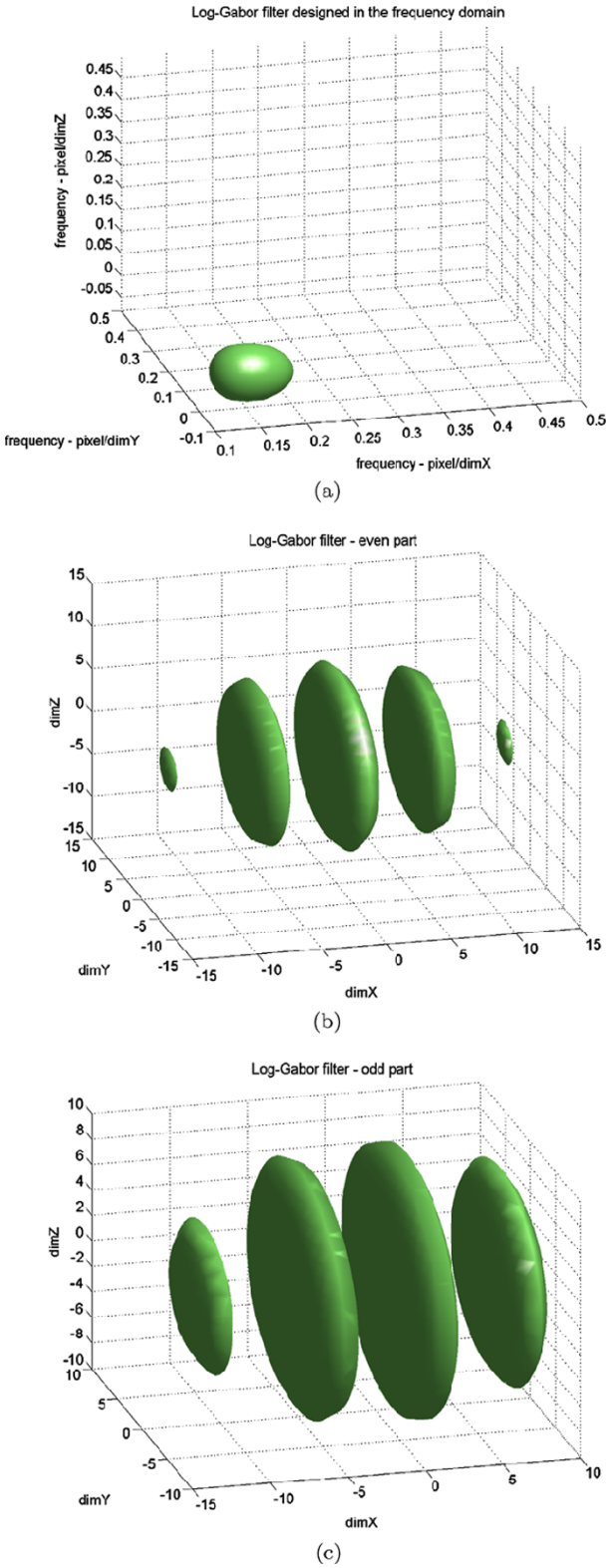

Fig. 3 Example of a 3D log-Gabor filter used in this work. (**a**) Filter designed in the frequency domain and the corresponding isosurfaces from the even (**b**) and odd (**c**) wavelet components in the spatial domain. Due to the lack of analytical representation of the log-Gabor filter, the wavelet representations in (**b**) and (**c**) were obtained by inverse Fourier transform of the filter in (**a**). Plot in (**a**) shows the frequency response of a 3D log-Gabor filter for a 80% decay of its energy

the support area, where the energy of the coefficients are significant,[2] is determined automatically during the filter design and only the rectangular region encapsulating the support area is saved to a disc file for further use. When filtering an image, the filters are loaded one-by-one from the disc into the computer memory and the filtering process is executed as described previously.

The proposed method was implemented in C++ language and the FFT computations were performed using the FFTW 3.2.2 library [12]. All results reported in this paper were obtained using a desktop personal computer with a Pentium IV single-core (3.4 GHz) processor and 1 GB of memory.

3.1.2 Design strategy and parameters tuning

The bank of filters should be designed to cover the log-frequency plane uniformly with a minimal overlap between the filters. In other words, the transfer function should be as close as possible to a perfect bandpass filter. Depending on the application, the bank of filters may be designed to better respond to oriented structures in an image (anisotropic filters). In the present work, the filters were designed to give approximate isotropic responses, since the image structures do not present any preferential orientation.

By appropriately setting the constant η_β, and the number of scales (S), elevations (N_e) and azimuths ($N_{a,0}$), it is possible to change the spectrum coverage of the filters. An important aspect of the design is to set the value of the highest filter centre frequency smaller than the Nyquist frequency to that to avoid aliasing artifacts. Granlund and Knutsson [14] suggested that the maximum frequency centre should follow the condition $\omega_{\max} < 0.5 \cdot \eta_\beta^m$, with $m = 3$ being the number of standard deviations.

Experimentally, it was found that a very reasonable uniform spectral coverage, as indicated by Figs. 1 and 2(b), can be obtained by fixing the maximum radial frequency centre of the filters to $\omega_{\max} = 0.15$ cycles/width and setting $\eta_\beta = 0.745$, which gives a filter bandwidth of approximately 1 octave. The number of azimuth angles on the equator of the sphere and the number of elevations angles were set to $N_{a,0} = 6$ and $N_e = 4$, respectively. The number of scales was set to $S = 3$ and the angular standard deviation to $\sigma_\alpha \approx 25°$. The central frequency of each scale is defined as $\omega_i = \omega_{\max}/2^{S-1}$.

Although there is no exact formula or recipe for the adjustment of these parameters, five important points were taken into account in the design of the bank of filters: (1) the quality of PC map, in the sense of better feature localization, improves as the number of scales increases; (2) the number of elevations depends on the in-plane resolution—the higher the in-plane resolution is, the finer the elevation sampling should be; (3) the number of azimuths in the equator of the sphere is related to the through-plane resolution—the higher the through-plane resolution is, the finer the angular (azimuth) sampling should be; (4) the parameters were set by taking into account the trade-off between quality of the PC map and the computational time required to process an image; (5) filters with wavelengths greater than half of the smaller dimension of the original image were discarded, as they approximately represent the average intensity level.

Because the through-plane sampling rate in the Computed Tomography (CT) images used in this work is 1.5 times higher than the in-plane rate, a correction factor was applied to the z coordinate in the filter design to solve this discrepancy. One important property of the Fourier transform that should be noticed is that frequency expansion in the spatial domain results in contraction in the Fourier domain. Therefore, in the present work, we have set $\omega' = \omega/1.5$, which represents the frequency in z direction is contracted by 1.5 times.

3.2 Detection of landmarks

The procedure for detection of 3D landmarks starts by first convolving the original image with the designed bank of 3D log-Gabor filters described in Sect. 3.1. Then the resulting filtered images are used to compute the phase congruency measure independently for each orientation $\Theta = \{\theta, \phi\}$ and at each position $\mathbf{s} = (x, y, z)$ in an image by using (1). The phase congruency is a dimensionless quantity, which is invariant to intensity and contrast variations and, therefore, it is possible to use its magnitude directly to determine the significance of a feature at each point in an image. In fact, if the phase congruency values are squared and normalized for the number of orientations used on the filter design, then the values will correspond to phase congruency moments ranging from 0 to 1 [21]. Consequently, from the theory of wavelets [27] and discrete image moment analysis [25], a 3D phase congruency moment of order $p + q + r$ computed for each pixel in an image can be written as

$$M_{p,q,r}(\mathbf{s}) = \sum_n \sum_\Theta x_{n,\Theta}^p \cdot y_{n,\Theta}^q \cdot z_{n,\Theta}^r, \tag{9}$$

where

$$\begin{aligned} x_{n,\Theta} &= \mathrm{PC}_n(\mathbf{s}) \cdot \cos\theta \cdot \cos\phi, \\ y_{n,\Theta} &= \mathrm{PC}_n(\mathbf{s}) \cdot \cos\theta \cdot \sin\phi, \\ z_{n,\Theta} &= \mathrm{PC}_n(\mathbf{s}) \cdot \sin\phi \end{aligned} \tag{10}$$

and n and Θ are the indices for the number of scales and the total number of orientations, respectively. From (9), a 3×3 symmetric matrix of second-order moments of inertia can be

[2] A coefficient is considered to be significant if its value is higher than 20% of the energy peak of the filter.

written as

$$M_{\mathrm{PC}}(\mathbf{s}) = \begin{bmatrix} M_{200}(\mathbf{s}) & M_{110}(\mathbf{s}) & M_{101}(\mathbf{s}) \\ M_{110}(\mathbf{s}) & M_{020}(\mathbf{s}) & M_{011}(\mathbf{s}) \\ M_{101}(\mathbf{s}) & M_{011}(\mathbf{s}) & M_{002}(\mathbf{s}) \end{bmatrix}. \tag{11}$$

The principal axis, corresponding to the axis about which the moment is minimized, provides an indication of the orientation of the feature in the image [21]. Similarly to the 2D case, the magnitude values of the image moments about the axes perpendicular to the principal axis give an indication of the significance of the feature in 3D. If these values are large in addition to the minimum moment, this indicates that the feature point has a strong 3D component associate to it, and consequently, it should be classified as a landmark point. Instead of computing directly the principal moments of inertia, they can be approximated by the eigenvalues of the second-order 3×3 matrix of moments in (11). The eigenvalues of this symmetric matrix, represented in an ordered manner by $\lambda_1 \geq \lambda_2 \geq \lambda_3$, are real-valued and positive values and they are related to the shape of an ellipsoid with the lengths of its semiaxes being proportional to the eigenvalues. When all three eigenvalues are sufficiently large, this indicates a point-like structure. Therefore, in the present work, a 3D landmark point is identified by using a quantity computed in terms of the eigenvalues for each position $\mathbf{s}$ as follows

$$R(\mathbf{s}) = \frac{\lambda_1 \cdot \lambda_2 \cdot \lambda_3}{\sqrt{\lambda_1^2 + \lambda_2^2 + \lambda_3^2}}, \tag{12}$$

where, the denominator of the equation is a normalization factor used to avoid the detection of the landmarks only on high contrast regions.

Figure 4 illustrates the axial, frontal, and sagittal views of a 3D map obtained by using (12). The landmarks are then detected on this map as 3D local maxima points by using a kernel with size adaptable to the scale of the salient feature in which the normalized energy response of the log-Gabor filters is the highest. In this work, kernel sizes of 15, 13, and 11 pixels were used, respectively, for the large, middle, and small scales.

3.3 Computational complexity analysis

In this section, we provide the computational complexity analysis of our proposed algorithm for the detection of point landmarks in 3D medical images. Here, we will discuss an algorithm that exploits some, but not necessarily all of the available manners to reduce the computational complexity. Since the computation of the bank of Gabor filters is performed off-line, i.e., all filters are computed only once and saved in a disc for further use, then the complexity analysis of the time and space discussed as follows consider only the worst case scenario of the image filtering procedure. In 3D imaging techniques, an image is represented as a volume of size $N_x \times N_y \times N_z$, where N_z is the number of slices and N_x and N_y correspond to the dimensions of the in-plane matrix. In radiation therapy practice of head and neck, it is uncommon to use isotropic image sampling and image matrix with dimension higher than 512 pixels. In general, the images are represented by a matrix of 256×256 or 512×512 pixels with the number of slices varying from 64 to 256, which is sufficient to cover the entire anatomical area with a good trade-off between image quality, spatial sampling and acquisition time. For the sake of analysis and notation simplicity, in this work we assume that $N = N_x = N_y = N_z$. However, it is important to note that the signal size N in this case has an upper bound and it will not grow unlimited.

Our image filtering algorithm starts by computing the DFT of the input image using the FFT algorithm implementation proposed in [12]. For a one-dimensional signal with size N, the direct (or inverse) FFT requires only $O(N \log N)$ real operations, independently of the signal length. Therefore, for an image of size N^3, the total complexity is $O(N^3 \log N)$ [12]. The second step is to compute the complex product of the transformed input image and a real-valued Gabor filter, designed directly in the frequency domain. Because of the transforms are Hermite [16], we need only to record (and multiply) half of that many values, i.e., only one side of the spectrum will be modified. In addition, as mentioned in Sect. 3.1.1, only the support region of each 3D filter with size $M_x \times M_y \times M_z$ needs to be multiplied to the complex data from the transformed input image. Similarly to the image dimensions, for the sake of simplicity we have considered $M = M_x = M_y = M_z$. Although the support region of the filter varies with the input image size, its dimensions are much smaller than the image dimensions, i.e., $M \ll N$. Since the values of the filters are all real, each nominal complex multiplication requires only two real multiplications, $O(M^3)$. Afterward, the product must be inverse transformed, with order $O(N^3 \log N)$, and saved for posterior analysis. Thus, the total number of operations to filter an image using one filter of the bank is $O(N^3 \log N + M^3)$. This must still be multiplied by $S \times N_a \times N_e$, which is the total number of filters in the bank, and add $N^3 \log N$ operations due to the direct FFT of the input image. In the next and final step, the computation of the PC local energy and moment maps require both $O(N^3)$ operations. In conclusion, the time complexity of the proposed algorithm is

$$\begin{aligned} &T(N, M, N_e, N_a, S) \\ &\quad = O\left(N^3 \log N + \left(N^3 \log N + M^3\right) N_e N_a S + N^3\right) \\ &\quad = O\left(\left(N^3 \log N + M^3\right) N_e N_a S\right) \\ &\quad = O\left(N_e N_a S N^3 \log N\right). \end{aligned} \tag{13}$$

Although the number of scales, azimuths, and elevations were set to fix values in this work, they may be slightly

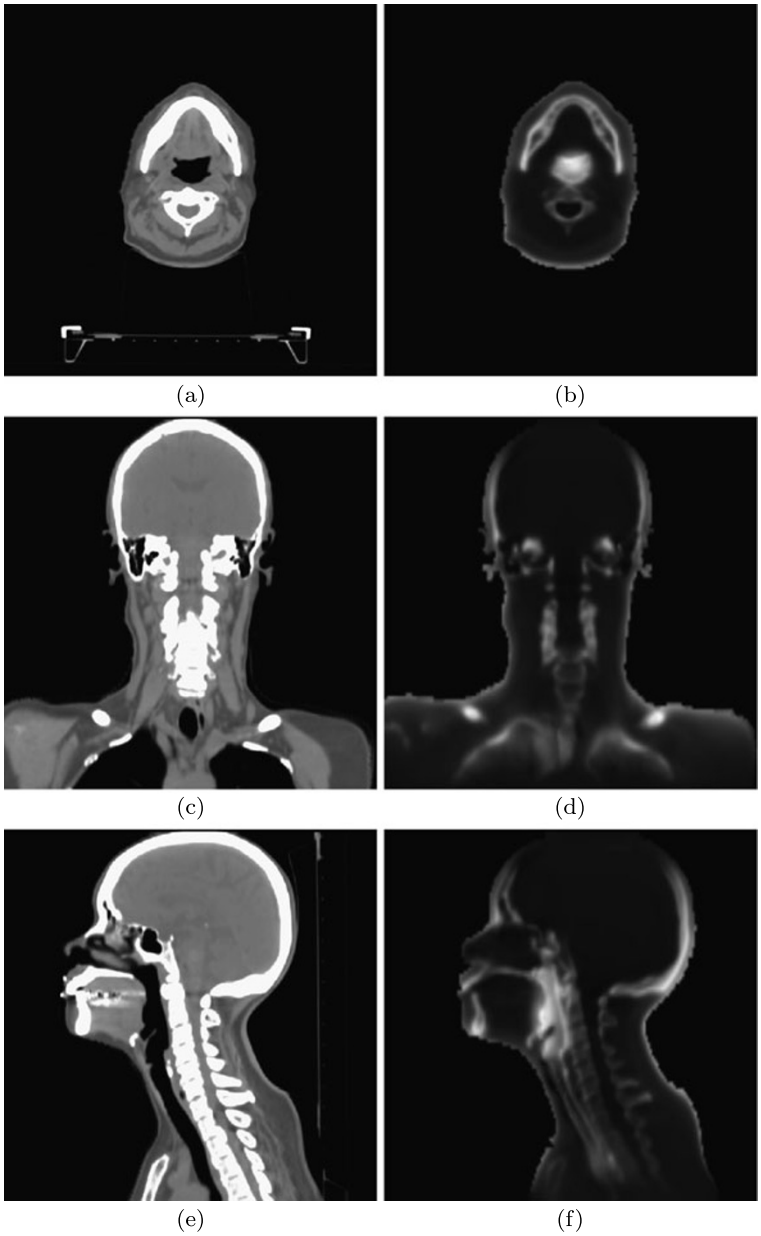

Fig. 4 Axial (**a**, **b**), coronal (**c**, **d**) and sagittal (**e**, **f**) image CT views for the original image (*left column*) and the respective eigen-maps obtained by using (12) (*right column*). Image contrast was modified for the sake of best visualization

changed depending on the image characteristics. Therefore, they were also considered in the complexity analysis.

In our experiments using the personal computer described in Sect. 3.1.1, the average processing time of an image of size $256 \times 256 \times 98$ is about 2 min.

A space complexity analysis was also performed for the proposed method. The image filtering step requires additional memory to hold two complex images with $O(N^3)$ each; one for the FFT of the original image and a second image to keep the resulting multiplication of the transformed image and a Gabor filter. Memory space to load a Gabor filter from the disc is also required, $O(M^3)$. The required memory space to compute the PC local energy map is $O(N^3)$, which is mostly used to hold temporary data in the implementation of (1). The most memory consuming part of the proposed algorithm is where the minimum moment map is computed. For this computation, the additional required memory is $O(N^3)$. Therefore, the total space required by the proposed algorithm is

$$Sp(N, M) = O\left(N^3 + M^3 + N^3\right) = O\left(N^3\right). \tag{14}$$

3.4 Phase congruency measure applied to MR images

In the current work, we have emphasized that one of the most important characteristics of the PC measure applied to detection of 3D point landmarks in medical images, in comparison to gradient based methods, is the fact that this

measure is invariant to intensity parameters. In this section, a very simple experiment is presented to illustrate such important property. Although in radiotherapy planning, which is the main application of our proposed method in this work, computed tomography (CT) is still the most common imaging modality used in practice, multimodality fusion [45], such as CT and Magnetic Resonance Imaging (MRI) and CT and Positron Emission Tomography (PET), has become an important procedure to more thoroughly investigate tumors in the head-neck anatomy [42].

Despite the great success of the MRI in radiation therapy, MR images present an intrinsic artifact called "bias field." Such an artifact is inevitable in the imaging processes due to a number of factors including the imperfection of magnetic fields and inhomogeneous properties of scanned object. The majority of intensity inhomogeneities appears as a low-frequency intensity variation known as bias field across the whole image from slice to slice. The intensity inhomogeneities may reach up to 40% of the intensity amplitudes. Although it may be unnoticeable to the eye, the spurious intensity variation may significantly hamper the precise measurement in automated MRI image segmentation, registration, qualification, or other quantitative image analyses based on intensity levels, which usually rely on the assumption that a specific tissue is represented in similar intensity throughout the data [13].

Figure 5(b) shows a simulated MR image obtained from the BrainWeb project [5] which is corrupted by noise and intensity inhomogeneity, showed in Fig. 5(a), due to the bias field phenomenon. As it can be easily seen in Fig. 5(c), thresholding or intensity-based classification are highly affected by this artifact. Gradient-based edge detectors are also greatly affected in the sense that setting a global threshold on gradient strength becomes more difficult, as intensity differences also vary locally. This effect is shown in Fig. 5(d). On the contrary, the phase congruency method seems to be very robust to the presence of intensity variations across the image, as shown in Fig. 5(e).

3.5 Manually annotated versus automatically detected landmarks

For the sake of illustration, Fig. 6 shows two examples of results obtained from the proposed method in comparison to patient-invariant point landmarks manually annotated by an expert radiation oncologist (JK). Points in red (dark gray in printed version) indicate the landmarks automatically detected by our method and points in yellow (light gray in printed version) are the landmarks manually annotated. Large points correspond to landmarks in the plane of view and the blue arrows indicate good correspondence matches between the landmarks. The C7 vertebra is indicated in the image for the sake of better understanding of the three different planes of view used in the illustrative example.

As it can be noticed, the number of detected points is greater than the annotated ones. The reason is that, due to the intense required labor work, only a few anatomical important point-landmarks were manually annotated in the CT images and considered for comparison in this work. Besides, the number of automatically detected landmarks is controlled by a threshold value and, in this work, was set to detect 200 landmarks. Due to a good image contrast present in the cervical spine and mandible regions of the CT images, a large number of landmarks was properly and consistently detected in the images. Despite the low contrast of the structures in the soft-tissue areas of the anatomy, a considerable number of landmarks was also detected in these regions. Even using a relatively high threshold to select the detected landmarks, it can be seen in Fig. 6 that the algorithm is very robust to avoid detecting curvilinear structures with high contrast, such as the skull contour. Another important point to be noticed in Figs. 6(a)–(d) is that the detected landmarks present a relatively large degree of symmetry, which is in agreement with the almost symmetric nature of the head-neck anatomy.

Visual comparison between the landmarks manually annotated and the ones automatically detected is only presented to demonstrate that the proposed method in fact can detect landmarks that are anatomically meaningful. It should also be noticed that the proposed method uses only image information in order to detect the landmarks, while a radiation oncologist uses both image information and his/her anatomy expertise to annotate the landmark points.

4 Application of the proposed algorithm to radiation therapy planning

The aim of radiation therapy (RT) is to accurately deliver maximum radiation dose to the target tumor volume while optimally sparing the normal tissue [48]. Accurate tumor and organ at risk delineation is a very important required procedure in the RT planning process. Traditionally, organ contouring for radiation treatment planning is performed manually on 2D axial CT image slices using simple drawing tools. This process is extremely labor intensive and can take many valuable hours of clinician's time. In addition, recent advances in RT such as the transition from conformal methods to intensity-modulation RT methods and the introduction of 4D CT and adaptive radiotherapy have further amplified the burden of an organ delineation [26]. The development of robust and reliable automatic or semi-automatic segmentation techniques has the potential to substantially facilitate the planning process and significantly increase the patient throughput in the clinic [49]. This is specially important in the head and neck RT planning, where the number of contours that need to be drawn is very large due to the complexity of this anatomy.

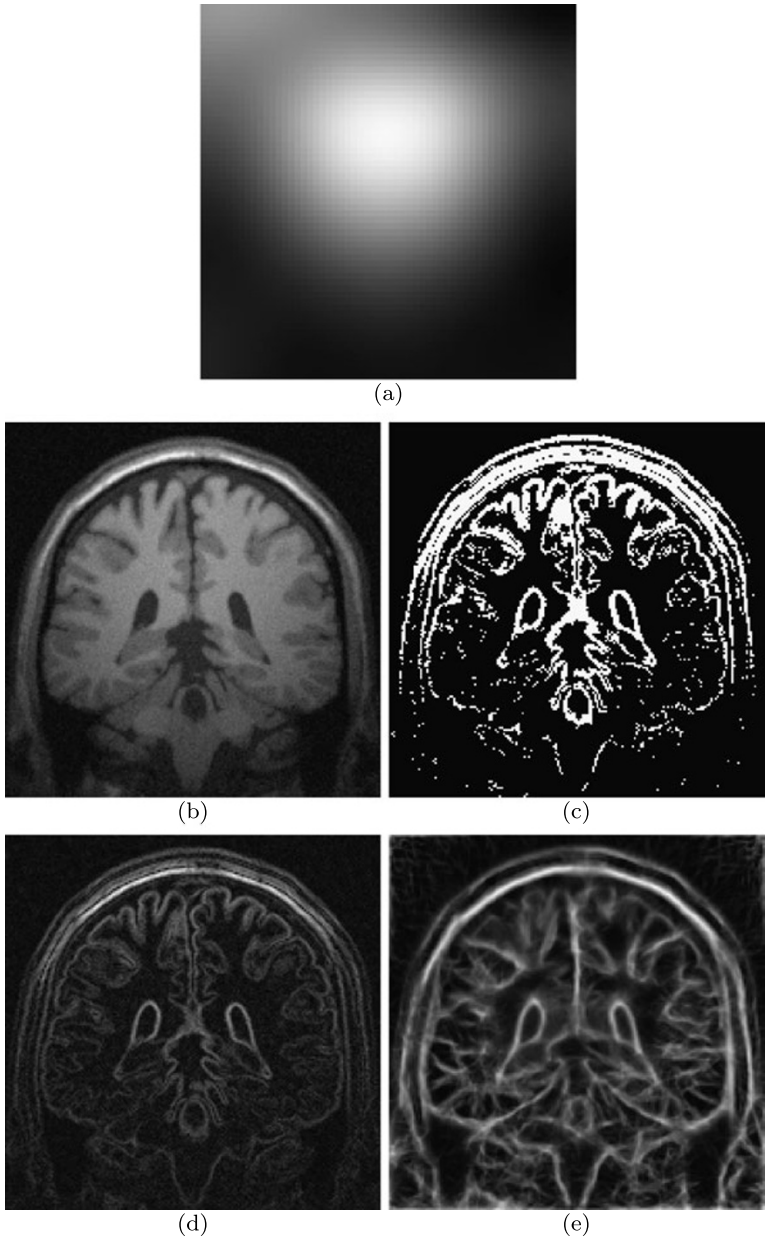

Fig. 5 (**a**) Bias field map function corrupting the MR image in (**b**). The image was contrast enhanced for the sake of better visualization; (**b**) corrupted MR image; (**c**) Resulting image after applying Otsu thresholding [34] to (**b**); (**d**) gradient magnitude; (**e**) phase congruency map

Recently, various image processing techniques have been proposed in the literature to aid radiation oncologists in delineation of anatomy [15, 44]. Among them, deformable models have been showing to be one of the most suitable approaches for this specific task since they allow the general shape, location, and orientation of the anatomical structures of interest in the image to be incorporated in the segmentation procedure [35]. Particularly, this is an important advantage to segment soft tissue structures in CT data, where image contrast is usually very poor. In addition, they are robust to image noise and artifacts due to their inherent continuity and smoothness properties.

In the current work, two different application scenarios are used to illustrate the feasibility and usefulness of the proposed method for detection of 3D landmarks. In the first example in Sect. 4.1, the method is used to initially positioning deformable models in planning CT images. In the second example in Sect. 4.2, the method is used to propagate normal tissue planning contours from the planning CT to multifraction Cone-Beam Computed Tomography (CBCT) volumes.

4.1 Initialization of deformable contours

The ability of deformable models to effectively segment organs of interest is in part dependent on their proper initialization (initial positioning) in the dataset of interest. For example, automatic initialization of the models can be done by nonrigid registration of a patient dataset and an atlas dataset

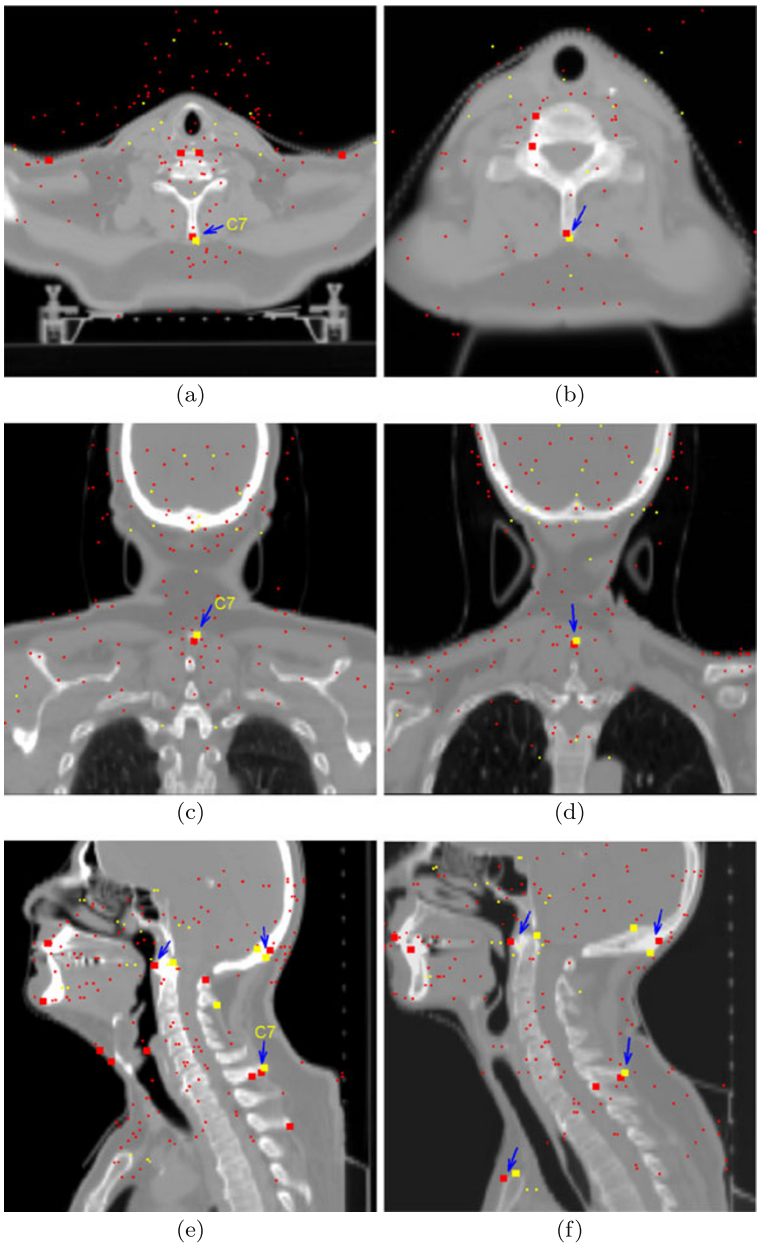

Fig. 6 Comparison between manual annotated and automatically detected 3D landmarks for CT images of two different patients. (**a**) Axial, (**b**) frontal and (**c**) sagittal CT views showing in *red* (*dark gray* in printed version) the landmarks automatically detected and in *yellow* (*light gray* in printed version) the landmarks manually annotated. Landmarks located in the plane of view are indicated by *large dots*

containing ground-truth contours. By applying the transformation between the atlas and the patient, the models can be propagated to the patient dataset of interest [22]. However, robust nonrigid interpatient deformable image registration is a very challenging task in radiation therapy planning due to the high anatomical variability, as well as image artifacts, which are mostly caused by dental fillings or metal implants.

In the present work, the proposed 3D PC landmark detection method was used to guide a landmark-based registration algorithm applied for initialization of deformable organ models in the head and neck area. The method starts by first computing an initial 3D thin-plate spline (TPS) transformation [2] using an atlas-based method proposed by Leavens et al. [22]. Next, a total of two hundred landmarks, as illustrated in Fig. 7, is automatically detected on the reference CT image using our proposed 3D PC landmark detection method. From those, a small subset of landmarks (42 in this example) is automatically selected based on the distances of the landmarks to the models of interest (brain, brain stem, mandible, and spinal cord), represented by triangular meshes. Only landmarks located within 2–10 mm of distance, depending on the organ, were kept for further processing. Finally, the Levenberg–Marquardt algorithm [28] is used to optimize the initial TPS transformation obtained from the atlas-based registration. The sum of squared differences of pixel values inside a small rectangular mask placed around each detected landmark is used to evaluate image similarity for the optimization. For the purpose of compar-

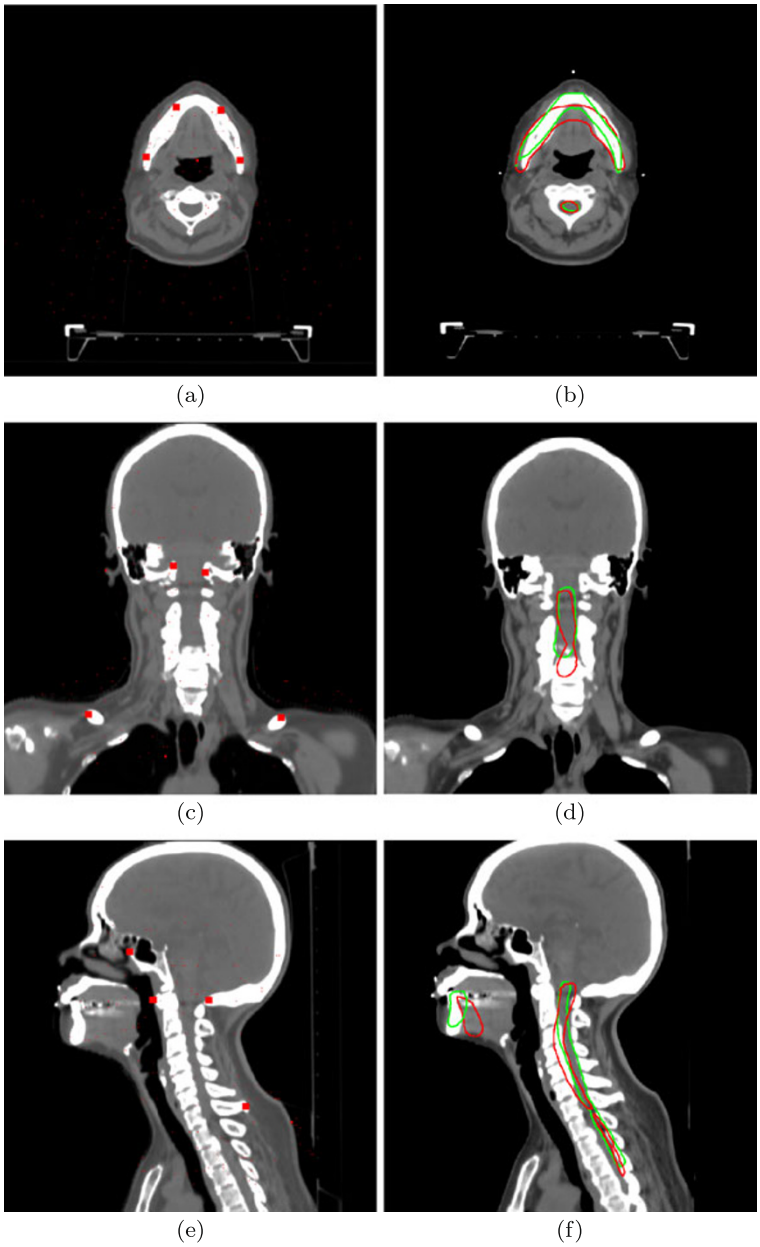

Fig. 7 Results of the proposed algorithm for deformable contour initialization. *Left column*: PC-landmarks overlaid on the original axial (**a**), coronal (**c**) and sagittal (**e**) CT view images. *Right column*: initial placed contours obtained by using the *gray-level* intensity (*red* or *dark gray* in printed version) and PC-map (*green* or *light gray* in printed version) as a measure of image similarity. Landmarks located in the plane of view are indicated by *large dots*

ison, two sources of image information were used in this work to measure image similarity: the gray-level intensity and the computed PC map.

Figure 7 shows a CT image of a patient with the mandible and spinal cord contours overlaid on the axial, sagittal and coronal images. The red (dark gray in printed version) contours were obtained by using the gray-level intensity as image similarity in the optimization algorithm while the green (light gray in printed version) contours were obtained by using the PC map. Landmarks obtained from the proposed 3D PC landmark detection algorithm were used in both cases. By visually assessing the images in Fig. 7, it can be easily noticed that the use of the PC map has improved significantly the placement of the initial contours. This can be explained by the fact that the landmarks used to drive the positioning of the contours correspond to prominent features in the image highlighted by the PC map (see Figs. 4 and 7 for comparison), which helps the optimization algorithm to converge to a better local minimum.

4.2 Automatic head-neck contour propagation

In image-guided adaptive radiation therapy, multiple additional images of a patient are acquired to verify the setup and monitor the progress of the radiation treatment. In particular, CBCT on-board imaging devices have become standard tools for image-guided procedures. The aim of adaptive treatment is to detect deviations from the original plan

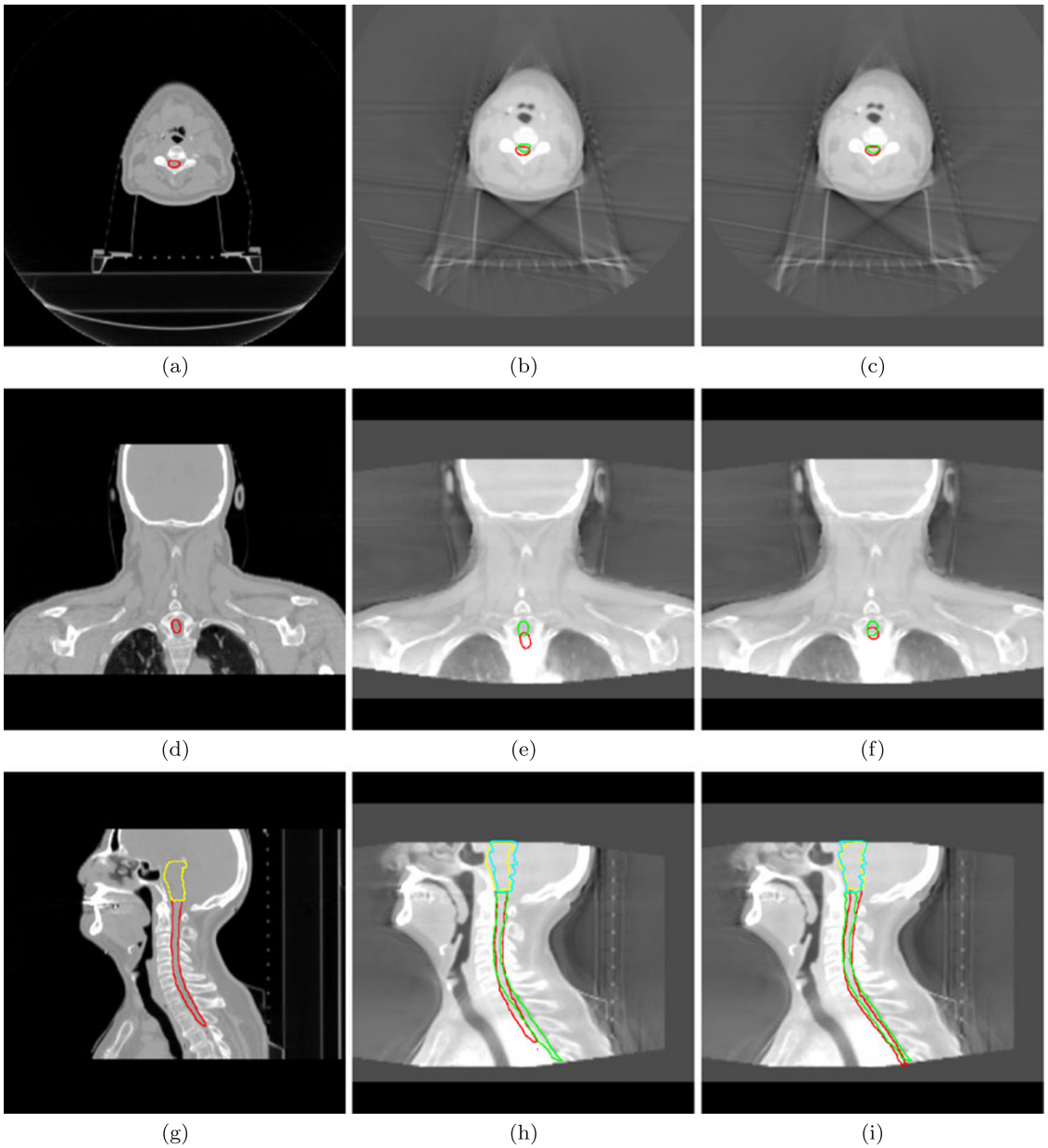

Fig. 8 Results of contours propagation from a CT planning image to a CBCT fraction. *Left column*: spinal cord (*red* or *dark gray* in printed version) and brain stem (*yellow* or *light gray* in printed version) contours manually delineated in a CT image. *Middle column*: contours from the CT copied to the CBCT image. *Right column*: contour propagation from CT to CBCT image using the 3D PC-landmarks. *Green* and *light blue* contours (or *light gray* tones in printed version) are the truth contours manually annotated on the CBCT images and used for the purpose of quantitative and visual comparison

at an early stage and perform corrections if needed. Therefore, the original delineations from the planning CT image need to be transferred to the follow-up datasets. When using daily CBCT imaging, this procedure can only be successfully accomplished by using automated methods due to the large amount of images. In addition, manual contouring on CBCT images is often infeasible due to the very poor soft tissue discrimination.

In this work, we have used PC landmarks to automatically transfer contours from planning CT to CBCT images. The method starts by detecting a total of 300 landmarks on a planning CT image using the proposed 3D PC landmark detection algorithm. Then the detected landmarks are retrieved in the CBCT fraction images by using maximum local correlation within a small searching area [1]. A threshold value of 0.7 applied to the correlation coefficients ranging from 0 to 1, and a search area of 30×30 mm^2 were used in this

Table 1 Average and percentile distances resulting from the quantitative analysis of the contour propagation method applied to six patient datasets

	Copied contours (mm)		TPS/PC-landmarks (mm)	
	spinal cord	brain stem	spinal cord	brain stem
average dist.	4.00	3.57	2.66	3.23
10%	0.10	0.02	0.09	0.03
20%	0.19	0.05	0.16	0.07
30%	0.26	0.12	0.23	0.12
40%	0.34	0.22	0.30	0.21
50%	0.44	0.33	0.38	0.32
60%	0.57	0.47	0.47	0.44
70%	0.87	0.72	0.60	0.70
80%	1.38	1.51	0.81	1.28
90%	2.47	3.47	1.68	2.69
100%	11.48	8.35	9.55	8.02

work. Finally, the contours are propagated from the CT to the CBCT images by using the TPS interpolation method anchored on the detected point correspondences [2].

For the evaluation of the proposed method, two contours of normal structures (spinal cord and brain stem) drawn in the initial planning CT were propagated to a CBCT image at each fraction using the same patient setup. Figure 8 shows in the left column the axial, coronal and sagittal views of a planning CT image with the overlaid manually drawn contours. The middle and the right columns show the CBCT image views with the contours transferred, respectively, by copying the original contours and using the TPS interpolation method anchored on the matching 3D PC landmarks. Manually annotated contours drawn by an expert radiation oncologist (AH) in green and light blue colors (or light gray tones in printed version) on the CBCT image are presented for visual comparison of volumetric concordance. By comparing the overlaid contours in the image views in Fig. 8 (middle and right columns), one can easily notice that the automatically propagated contours (right column) are much closer to the ground truth comparing to the copied contours (middle column). The effectiveness of the proposed method was also quantitatively assessed by measuring the distances between the propagated contour vertices to the ground truth meshes of the respective structures for six different patient datasets, as shown in Table 1. For both structures, the spinal cord and brain stem, the average distances obtained by using the automatic TPS/PC landmarks method were smaller than the distances obtained by copying the contours. For the brain stem, the automatic TPS/PC landmarks method has only shown a slightly improvement over the contour copy (3.23 mm versus 3.57 mm average). This can be explained by the fact that brain stem usually does not undergo large deformations. Furthermore, the lack of image contrast in this area makes manual image contouring a very difficult task and can introduce bias to the comparison. In contrast, the automatic method has performed considerably better in the spinal cord region (2.66 mm versus 4 mm average).

In addition to the average distances, the percentile distances, as shown in Table 1, were computed after sorting all vertices distances in an ascending order. A percentile is the value of a variable below which a certain percentage of observations fall. For instance, the 10th percentile is the value (or score) below which 10% of the observations (the vertices distances in our case) may be found. As it can be noticed by comparing the percentile distances in Table 1, the method for automatic propagation of the contours has shown a better overall performance.

5 Conclusions

We have presented a new method for automatic detection of 3D image landmarks in volumetric medical images based on the phase congruency model. The method is very flexible in allowing multiresolution and oriented feature analyses. It is also adaptable to anisotropic image resolution, commonly present in medical images. The usefulness of the proposed method was demonstrated qualitatively and quantitatively by using two practical and important applications in radiation therapy planning; (a) initialization of deformable organ models and (b) automatic contour propagation between CT and CBCT images. By using local energy information instead of the magnitude of the intensity gradient in an image, the proposed method has a great potential to MR imaging applications, since MR images are usually affected by image intensity inhomogeneities. In addition to the proposed method for detection of 3D point-landmarks, 3D low-level image symmetries can be identified by slightly modifying (1). This information maybe used to detect 3D point-landmarks of a different nature.

Acknowledgements The authors would like to thank the Princess Margaret Hospital/University Health Network, Toronto, Canada, and Philips Healthcare for providing the funding for this work. The authors would also like to acknowledge the valuable suggestions made by Márcia Aparecida Fernandes, Professor—Ph.D. of the Federal University of Uberlandia, on the complexity analysis of the proposed algorithm.

References

1. Allaire S, Kim J, Breen S, Jaffray D, Pekar V (2008) Full orientation invariance and improved feature selectivity of 3D SIFT with application to medical image analysis. In: MMBIA-2008, Anchorage, AK, USA, pp 1–8
2. Bookstein FL (1989) Principal warps: Thin-plate splines and decomposition of deformations. IEEE Trans Pattern Anal Mach Intell 11(6):567–585
3. Cao G, Shi P, Hu B (2006) Ultrasonic liver discrimination using 2-D phase congruency. IEEE Trans Biomed Eng 53(10):2116–2119
4. Cheung W, Hamarneh G (2007) N-sift: N-dimensional scale invariant feature transform for matching medical images. In: 4th international symposium on biomedical imaging: From nano to macro (ISBI) 2007, Washington, DC, USA, pp 12–15
5. Collins DL, Zijdenbos AP, Kollokian V, Sled JG, Kabani NJ, Holmes CJ, Evans AC (1998) Design and construction of a realistic digital brain phantom. IEEE Trans Med Imaging 17(3):463–468
6. Dosil R, Pardo XM (2003) Generalized ellipsoids and anisotropic filtering for segmentation improvement in 3-D medical imaging. Image Vis Comput 21(4):325–343
7. Dosil R, Pardo XM, Fdez-Vidal XR (2005) Decomposition of three-dimensional medical images into visual patterns. IEEE Trans Biomed Eng 52(12):2115–2118
8. Ferrari RJ, Hill KA, Plewes DB, Martel AL (2008) Can bilateral asymmetry analysis of breast MR images provide additional information for detection of breast diseases. In: XXI Brazilian symposium on computer graphics and image processing—SIBGRAPI 2008, Campo Grande, MS, Brazil, pp 113–120
9. Field DJ (1987) Relations between the statistics of natural images and the response properties of cortical cells. J Opt Soc Am A 4(12):2379–2394
10. Field DJ (1993) Scale-invariance and self-similar wavelet transforms: an analysis of natural scenes and mammalian visual systems. Oxford University Press, New York
11. Förstner W (1986) A feature based correspondence algorithm for image matching. Int Arch Photogramm Remote Sens 26(3):150–166
12. Frigo M, Johnson SG (2005) The design and implementation of FFTW3. Proc IEEE 93(2):216–231. Special issue on "Program Generation, Optimization, and Platform Adaptation"
13. Gispert JD, Reig S, Pascau J, Vaquero JJ, Garcia-Barreno P, Desco M (2004) Method for bias field correction of brain T1-weighted magnetic resonance images minimizing segmentation error. Hum Brain Mapp 22:133–144
14. Granlund G, Knutsson H (1995) Signal processing for computer vision. Kluwer Academic, Boston
15. Jaffray D, Brock KK, Ferrari R, Pekar V (2008) Applications of image processing in image-guided radiation therapy. Medica Mundi 52(1):32–39
16. Jähne B (1997) Digital image processing, 4th edn. Springer, San Diego
17. Kaus MR, Brock KK (2009) In: Deformable image registration for radiation therapy planning. Biomechanical system technology: computational methods, vol 1. World Scientific, Singapore, pp 1–28
18. Kitchen L, Rosenfeld A (1982) Gray-level corner detection. Pattern Recognit Lett 1:95–102
19. Kovesi P (1999) Image features from phase congruency. Videre, J Comput Vis Res 1(3):2–26
20. Kovesi P (2000) Phase congruency: A low-level image invariant. Psychol Res 64:136–148
21. Kovesi P (2003) Phase congruency detects corners and edges. In: The Australian pattern recognition society conference: DICTA, Sydney, Australia, December, pp 309–318
22. Leavens C, Vik T, Schulz H, Allaire S, Kim J, Dawson L, O'Sullivan B, Breen S, Jaffray D, Pekar V (2008) Validation of automatic landmark identification for atlas-based segmentation for radiation treatment planning of the head-and-neck region. In: Proceedings of the SPIE conference on medical imaging, vol 6914. San Diego, CA, USA, pp 3G1–3G7,
23. Linguraru MG, Marias K, English R, Brady M (2006) A biologically inspired algorithm for microcalcification cluster detection. Med Image Anal 10(6):850–862
24. Liu J, Gao W, Huang S, Nowinski WL (2008) A model-based, semi-global segmentation approach for automatic 3-d point landmark localization in neuroimages. IEEE Trans Med Imaging 27:1034–1044
25. Lo C-H, Don H-S (1989) 3D moment forms: Their construction and application to object identification and positioning. IEEE Trans Pattern Anal Mach Intell 11(10):1053–1064
26. Mageras GS, Mechalakos J (2007) Planning in the igrt context: closing the loop. Semin Radiat Oncol 17(4):268–277
27. Mallat S (1989) A theory for multiresolution signal decomposition: The wavelet representation. IEEE Trans Pattern Anal Mach Intell 11(7):674–693
28. Marquardt D (1963) An algorithm for least-squares estimation of nonlinear parameters. J Appl Math 11:431–441
29. McLoughlin KJ, Bones PJ, Kovesi PD (2002) Connective tissue representation for detection of microcalcifications in digital mammograms. Prog Biomed Opt Imaging 3(22):1246–1256
30. Monga O, Benayoun S (1995) Using partial derivatives of 3-D images to extract typical surface features. Comput Vis Image Underst 61(2):171–189
31. Morrone MC, Burr DC (1988) Feature detection in human vision: A phase-dependent energy model. Proc R Soc Lond B 235:221–245
32. Morrone MC, Owens RA (1987) Feature detection from local energy. Pattern Recognit Lett 6(5):303–313
33. Morrone MC, Ross JR, Burr DC, Owens RA (1986) Mach bands are phase dependent. Nature 324(6094):250–253
34. Otsu S (1979) A threshold selection method from gray-level histograms. IEEE Trans Syst Man Cybern 9(1):62–66
35. Pekar V, McNutt TR, Kaus MR (2004) Automated model-based organ delineation for radiotherapy planning in prostatic region. Int J Radiat Oncol Biol Phys 60(3):973–980
36. Pudney C, Kovesi P, Robbins B (1995) Feature detection using oriented local energy for 3D confocal microscope images. Image Anal Appl Comput Graph 1024:274–282
37. Rohr K (1997) On 3D differential operators for detecting point landmarks. Image Vis Comput 15(3):220–233
38. Ruiz-Alzola J, Kikinis R, Westin CF (2001) Detection of point landmarks in multidimensional tensor data. Signal Process 81:2243–2247
39. Shi XW (2010) GPU implementation of fast Gabor filters. In: Proceedings of 2010 IEEE international symposium on circuits and systems, Paris, France, June, pp 373–376
40. Slabaugh G, Kong K, Unal G, Fang T (2007) Variational guidewire tracking using phase congruency. In: Medical image computing and computer-assisted intervention (MCCAI) 2007, vol 4792, pp 612–619
41. Thirion J-H (1996) New feature points based on geometric invariants for 3-D image registration. Int J Comput Vis 18(2):121–137

42. Troost EGC, Schinagl DAX, Bussink J, Boerman OC, van der Kogel AJ, Oyen WJG, Kaanders JHAM (2009) Innovations in radiotherapy planning of head and neck cancers: Role of PET. J Nucl Med 51(1):66–76
43. Venkatesh S, Ownes R (1990) On the classification of image features. Pattern Recognit Lett 11(5):339–349
44. Wang H, Dong L, Lii MF, Lee AL, Crevoisier R, Mohan R, Cox JD, Kuban DA, Cheung R (2005) Implementation and validation of a three-dimensional deformable registration algorithm for target prostate cancer radiotherapy. Int J Radiat Oncol Biol Phys 61(3):725–735
45. Wong A, Bishop W (2008) Efficient least squares fusion of MRI and CT images using a phase congruency model. Pattern Recognit Lett 29(3):173–180
46. Wong A, Orchard J (2009) Robust multimodal registration using local phase-coherence representations. J Signal Process Syst 54:89–100
47. Wörz S, Rohr K (2006) Localization of anatomical point landmarks in 3-D medical images by fitting 3-D parametric intensity models. Med Image Anal 10(1):41–58
48. Xing L, Thorndyke B, Schreibmann E, Yang Y, Li T, Kim G, Luxton G, Koong A (2006) Overview of image-guided radiation therapy. Med Dosim 31(2):91–112
49. Xings L, Siebers J, Keall P (2007) Computational challenges for image-guided radiation therapy: Framework and current research. Semin Radiat Oncol 17(4):245–257